





Article

Ultrastable Conjugated Microporous Polymers Containing Benzobisthiadiazole and Pyrene Building Blocks for Energy Storage Applications

Mohamed Gamal Mohamed ^{1,2,†} , Tharwat Hassan Mansoure ^{2,†} , Maha Mohamed Samy ^{1,2}, Yasuno Takashi ¹, Ahmed A. K. Mohammed ², Tansir Ahamad ³, Saad M. Alshehri ³, Jeonghun Kim ⁴, Babasaheb M. Matsagar ⁵, Kevin C.-W. Wu ^{5,*}  and Shiao-Wei Kuo ^{1,6,*} 

¹ Center of Crystal Research, Department of Materials and Optoelectronic Science, National Sun Yat-sen University, Kaohsiung 80424, Taiwan; mgamal.eldin12@aun.edu.eg (M.G.M.); d083100006@nysyu.edu.tw (M.M.S.); yasanou21@hotmail.co.jp (Y.T.)

² Department of Chemistry, Faculty of Science, Assiut University, Assiut 71516, Egypt; tharout.mansour@science.au.edu.eg (T.H.M.); theoahmedkamel@gmail.com (A.A.K.M.)

³ Department of Chemistry, College of Science, King Saud University, Riyadh 11362, Saudi Arabia; tahamed@ksu.edu.sa (T.A.); alshehri@ksu.edu.sa (S.M.A.)

⁴ Department of Chemical and Biomolecular Engineering, Yonsei University, 50 Yonsei-ro, Seodaemun-gu, Seoul 03722, Korea; jeonghun.kim@uq.edu.au

⁵ Department of Chemical Engineering, National Taiwan University, No. 1, Sec. 4, Roosevelt Road, Taipei 10617, Taiwan; matsagar03@ntu.edu.tw

⁶ Department of Medicinal and Applied Chemistry, Kaohsiung Medical University, Kaohsiung 80424, Taiwan

* Correspondence: kevinwu@ntu.edu.tw (K.C.-W.W.); kuosw@faculty.nsysu.edu.tw (S.-W.K.)

† These authors contributed equally to this work.



Citation: Mohamed, M.G.; Mansoure, T.H.; Samy, M.M.; Takashi, Y.;

Mohammed, A.A.K.; Ahamad, T.; Alshehri, S.M.; Kim, J.; Matsagar, B.M.; Wu, K.C.-W.; et al. Ultrastable Conjugated Microporous Polymers Containing Benzobisthiadiazole and Pyrene Building Blocks for Energy Storage Applications. *Molecules* **2022**, *27*, 2025. <https://doi.org/10.3390/molecules27062025>

Academic Editors: Gauthier Ryzdzek, Qingmin Ji, Fabien Grasset and Amir Pakdel

Received: 2 March 2022

Accepted: 17 March 2022

Published: 21 March 2022

Publisher's Note: MDPI stays neutral with regard to jurisdictional claims in published maps and institutional affiliations.



Copyright: © 2022 by the authors. Licensee MDPI, Basel, Switzerland. This article is an open access article distributed under the terms and conditions of the Creative Commons Attribution (CC BY) license (<https://creativecommons.org/licenses/by/4.0/>).

Abstract: In recent years, conjugated microporous polymers (CMPs) have become important precursors for environmental and energy applications, compared with inorganic electrode materials, due to their ease of preparation, facile charge storage process, π -conjugated structures, relatively high thermal and chemical stability, abundance in nature, and high surface areas. Therefore, in this study, we designed and prepared new benzobisthiadiazole (BBT)-linked CMPs (BBT-CMPs) using a simple Sonogashira couplings reaction by reaction of 4,8-dibromobenzo(1,2-*c*;4,5-*c'*)bis(1,2,5)thiadiazole (BBT-Br₂) with ethynyl derivatives of triphenylamine (TPA-T), pyrene (Py-T), and tetraphenylethene (TPE-T), respectively, to afford TPA-BBT-CMP, Py-BBT-CMP, and TPE-BBT-CMP. The chemical structure and properties of BBT-CMPs such as surface areas, pore size, surface morphologies, and thermal stability using different measurements were discussed in detail. Among the studied BBT-CMPs, we revealed that TPE-BBT-CMP displayed high degradation temperature, up to 340 °C, with high char yield and regular, aggregated sphere based on thermogravimetric analysis (TGA) and scanning electron microscopy (SEM), respectively. Furthermore, the Py-BBT-CMP as organic electrode showed an outstanding specific capacitance of 228 F g⁻¹ and superior capacitance stability of 93.2% (over 2000 cycles). Based on theoretical results, an important role of BBT-CMPs, due to their electronic structure, was revealed to be enhancing the charge storage. Furthermore, all three CMP polymers featured a high conjugation system, leading to improved electron conduction and small bandgaps.

Keywords: conjugated microporous polymers (CMPs); benzobisthiadiazole; thermal stability; bandgaps; energy storage

1. Introduction

The news that the depletion of natural sources of energy has compelled researchers to search for alternatives that provide high energy and power density, long cycle life, good reversibility, and good sources of energy storage is not new. Among many other energy

storage systems (ESSs), the focus on supercapacitors has increased due to their high stability as a function of temperature, excellent cyclability, easy fabrication, high energy, and power density [1–7]. Supercapacitors store charge via two mechanisms—electrostatically and faradaically [1,7]. The electrostatic mechanism stores the charges at the interface of the supercapacitor electrode as electric double layer capacitance (EDLC), while the faradaic mechanism stores the charges at the electrode surface as pseudocapacitance (PC) due to the highly reversible surface redox reaction of the redox-active sites during charge and discharge [1,7]. The EDLC of the materials can be attributed to their surface areas. The materials that have high surface areas, such as carbonaceous materials, conjugated microporous polymers (CMPs), and covalent organic frameworks (COFs), usually have high EDLC [8–15]. It is, therefore, important to explore new electrode materials that synergize both EDLC and PC. With this in consideration, an ideal electrode material should meet several characteristics, such as having ideal redox-active sites, high specific surface area (SSA), good conductivity, suitable pore width, and good chemical and thermal stability, as well as being eco-friendly in nature. Extensive research on CMPs reveals that the introduction of heteroatoms (N, B, S, P) in the CMPs can be used to obtain materials with tunable pore size and PC [16–21].

In recent years, researchers across the globe have been dedicated—at both academic and industrial levels—to enhance the use of renewable and sustainable energy sources in order to limit the impact of fossil fuel resources on the environment [22]. Most commonly, polymers in polymeric electrolytes are categorized into synthetic and natural types; synthetic polymers such as polyethylene, polyvinyl chloride, polymethyl methacrylate, polycarbonate, and polyacrylonitrile are nondegradable and are of serious concern for environmental well-being [23]. Additionally, considerable progress has been achieved in the production of energy from renewable sources during the preceding two decades, which has triggered the need for both reliable and powerful energy resources while also being environmentally benign [24]. Recently, various biodegradable polymers such as cellulose, carbohydrates, and chitosan with appropriate modification to enhance their ionic conductivity have been employed as electrolytes in different energy storage devices such as batteries, dye-sensitized solar cells, and supercapacitors [25].

CMPs are porous compounds that are constructed from a covalent connection of π -conjugated building units that extended along with the skeleton, providing them 3D microporosity networks and especially high surface area at times [26–34]. They can be easily synthesized by using numerous C–C coupling reactions such as Yamamoto, Sonogashira, and Suzuki coupling, and also oxidative polymerization [35–44] which are characterized by a high degree of polymerization and crosslinking densities, as well as facilitates the incorporation of different moieties [45–50]. These coupling methods allow CMPs to highly possess CMPs to differentiate from other conventional polymers, with rapid ion/diffusion kinetics that originates from their individual porous properties [51–55]. Therefore, CMPs displayed high capacity and long-term cycling stability when they were applied as material electrodes in electrochemical energy storage applications [56–60]. Hence, they are considered as one of the ideal candidates for catalysis, gas storage, and electrochemical energy storage [61–64].

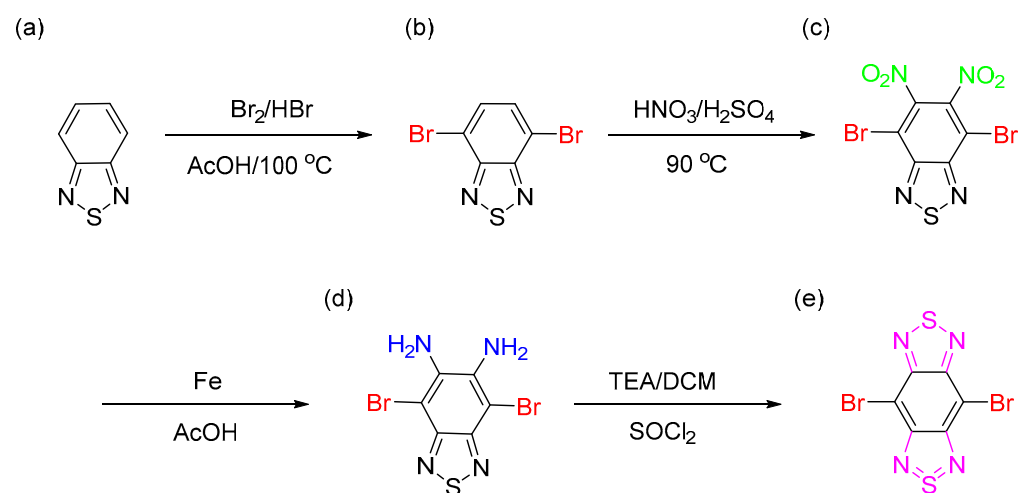
In recent years, benzobisthiadiazole moiety (BBT) is considered a strong withdrawing electron group and a promising molecule, which has widely been applied in organic photovoltaics, nonlinear optics, organic field-effect transistor, and organic light-emitting diodes, due to its charge carrier mobilities and low bandgap value [65–68]. This study is the first report to prepare CMP materials containing benzobisthiadiazole units and use these materials as an organic electrodes for supercapacitor application. Herein, we successfully constructed new BBT–CMPs containing benzobisthiadiazole, triphenylamine (TPA), pyrene (Py), and tetraphenylethene (TPE) moieties through Sonogashira coupling's reaction, and their structure and properties such as porosity, thermal stability, and surface properties were analyzed using solid-state NMR, scanning electron microscopy (SEM), transmission electron microscopy (TEM), and N_2 adsorption measurements. According to electrochemical data, our three new BBT–CMPs showed outstanding capacitance response

of up to 210 F g^{-1} with superior retention of capacity over long 2000 cycles. These results were associated with the theoretical studies, which were carefully carried out by using density functional theory (DFT), to calculate the distribution of different energy gaps such as the highest occupied molecular orbital (HOMO) and the lowest unoccupied molecular orbital (LUMO), and molecular electrostatic potential (MESP), respectively. Interestingly, the obtained theoretical results confirmed that the electronic structure of the BBT-CMP plays a critical role to improve charge storage. Furthermore, this study will pave the way for other applications such as hydrogen evolution and lithium batteries using BBT-CMPs due to their extended π -conjugation leading, small bandgaps, and highly delocalized LUMO distribution.

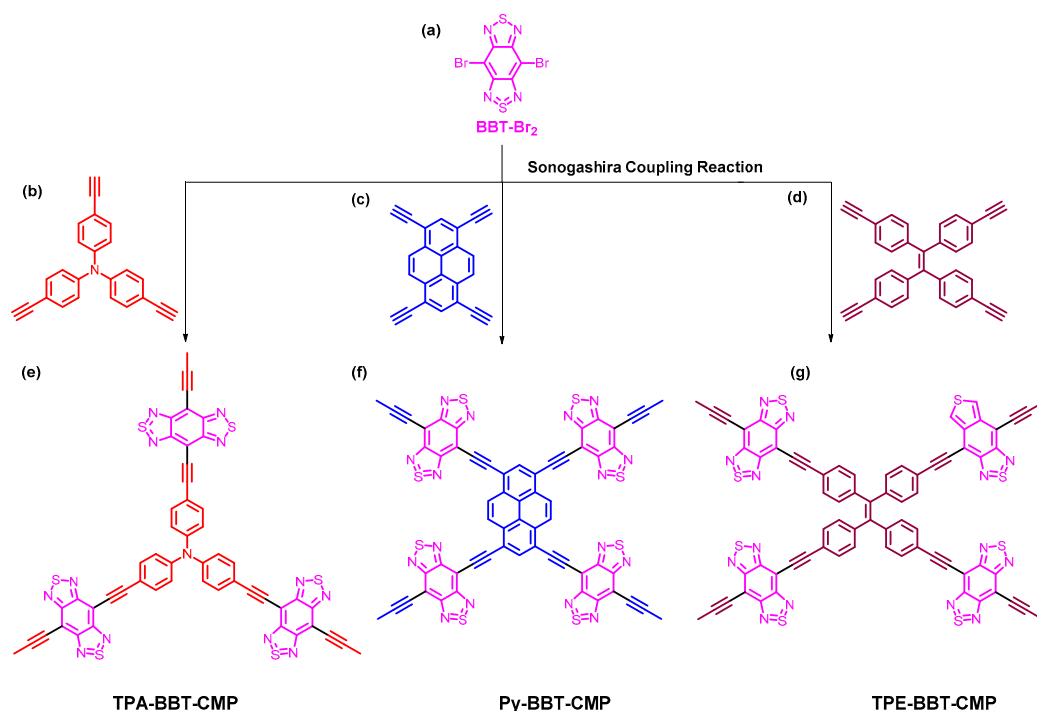
2. Results

2.1. Synthesis and Character of BBT Monomers and BBT-CMPs

BBT-Br₂ monomer was used as a building unit to prepare the different types of CMPs in this study for energy storage application, as displayed in Scheme 1. First, bromination reaction of 2,1,3-benzothiadiazole moiety (BT) (Scheme 1a) in the presence of aqueous solution HBr in acetic acid and Br₂ solution was made to afford BT-Br₂ as a white crystalline powder with a high yield of up to 85% (Scheme 1b). Then, we carried out the nitration reaction of BT-Br₂ by using both concentrated HNO₃ and H₂SO₄ to obtain BT-2NO₂, as displayed in Scheme 1c. The formation of BBT-Br₂ was successfully prepared through two steps by the reduction reaction of BT-2NO₂ in the presence of Fe powder in acetic acid solution to afford BT-2NH₂ (Scheme 1d), followed by ring closure reaction by using SOCl₂ in a mixture of triethylamine (TEA) and dichloromethane (DCM) to yield BBT-Br₂ (Scheme 1e) as a reddish-brown solid. The chemical formula of all of the synthesized monomers were confirmed by using Fourier transform infrared spectroscopy (FTIR), proton nuclear magnetic resonance (¹H-NMR), and mass spectroscopy analyses. The synthetic method for the synthesis of three novel CMPs based on the BBT unit is shown in Scheme 2e–g. The reaction of BBT-Br₂ (Scheme 2a) as the main building monomer with three different monomers containing alkynyl groups such as TPA-T (Scheme 2b), Py-T (Scheme 2c), and TPE-T (Scheme 2d) by using Sonogashira coupling reaction in the presence of Pd as a catalyst in DMF-TEA mixture (1:1) for 72 h to afford of TPA-BBT-CMP as a brown solid, Py-BBT-CMP as a reddish-brown powder, and TPE-BBT-CMP as an orange solid, respectively (Scheme 2e–g).



Scheme 1. Synthetic method of BT-Br₂ (b), BT-2NO₂ (c), BT-2NH₂ (d) and BBT-Br₂ (e) preparation from BT (a).



Scheme 2. Synthetic scheme of the TPA-BBT-CMP (e), Py-BBT-CMP (f) and TPE-BBT-CMP (g) from BBT-Br₂ (a), TPA-T (b), Py-T (c), and TPE-T (d).

Figure 1a represents the FTIR spectra of TPA-BBT-CMP, Py-BBT-CMP, and TPE-BBT-CMP, respectively. As observed in Figure 1a, all three BBT-CMP samples appeared corresponding absorption bands in the range of 3400, 2198, and 1624 cm⁻¹, corresponding to the stretching of OH group that belong to water absorption by CMP materials and stretching vibration of terminal C≡C and C=C groups, respectively. In addition, all BBT-CMPs featured absorption signals centered near 3045–3035 cm⁻¹ due to vibrations of the stretching aromatic C–H. The presence of aromatic carbon nuclei and internal C≡C signals in the three BBT-CMPs appeared in the range 116–146 ppm and 81 and 78 ppm as presented in ¹³C solid-state NMR (Figure 1b). In addition, the carbon nuclei of C=C units in the TPE moiety in the TPE-BBT-CMP spectrum were found to be 142 ppm. We evaluated the thermal stability of TPA-BBT-CMP, Py-BBT-CMP, TPE-BBT-CMP, and their corresponding monomers via TGA under the N₂ atmosphere from 100 to 800 °C (Figures 1c, S7, S11 and S15, Tables 1 and S1). The thermal decomposition temperatures at 10% weight loss (T_{d10}) and char yields were 256 °C and 15 wt% for BT-2NO₂; 228 °C and 0 wt% for BT-2NH₂; 262 °C and 13 wt% for BBT-Br₂. As shown in TGA profiles in Figure 1c, the weights of TPA-BBT-CMP, Py-BBT-CMP, and TPE-BBT-CMP remained constant up to 250 °C, with subsequent 10 wt% weight losses at 250, 244, and 347 °C, respectively; their char yields at 800 °C were 55, 48, and 67 wt%, respectively (Figure 1c). The powder X-ray diffraction (PXRD) measurements of all BBT-CMP samples exhibited amorphous character without possessing any ordered diffraction peaks, as illustrated in Figure 1d.

Table 1. A summary of the TGA and porosity properties of BBT-CMPs materials in this study.

Material	T _{d10} (°C)	Char Yield (%)	Surface Area (m ² g ⁻¹)	Pore Size (nm)
TPA-BBT-CMP	250	55	35.6	2.7
Py-BBT-CMP	244	48	67	1.3
TPE-BBT-CMP	347	67	410	1.8

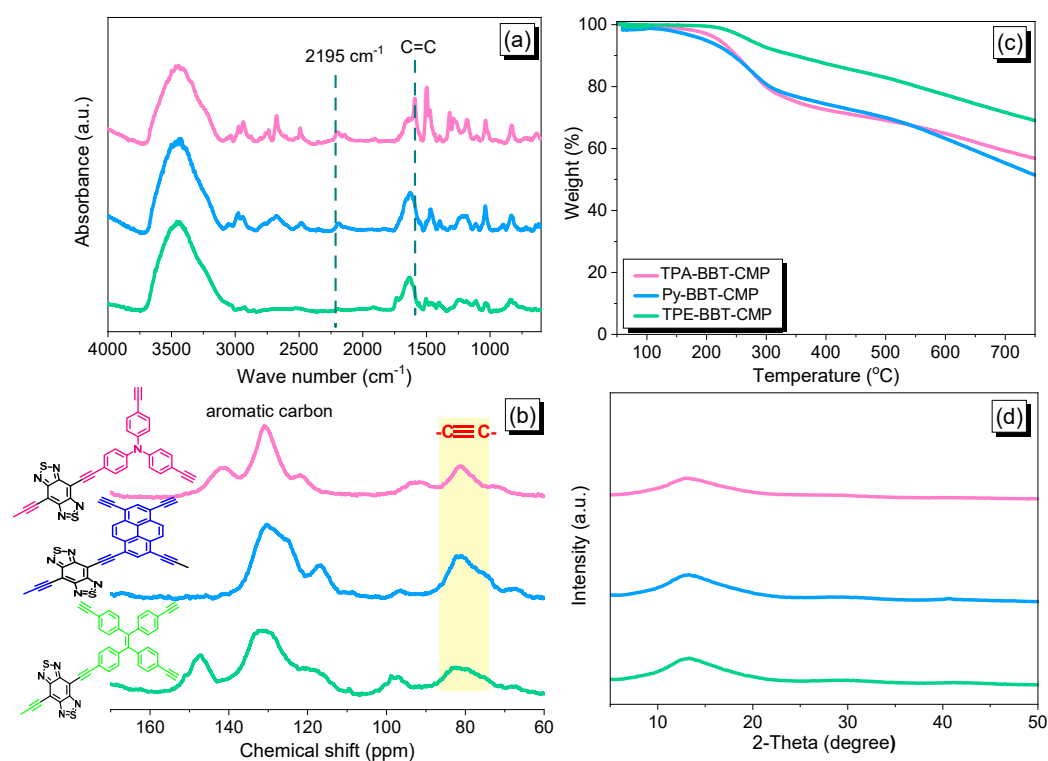


Figure 1. (a) FTIR, (b) TGA, (c) solid-state NMR, and (d) XRD spectra of the TPA-BBT-CMP, Py-BBT-CMP, and TPE-BBT-CMP.

2.2. Porosity and Morphologies Properties of BBT-CMPs

N_2 adsorption–desorption tests were performed at 77 K and 1 bar to corroborate the porosity characteristics of the TPA-BBT-CMP, Py-BBT-CMP, and TPE-BBT-CMP (Figure 2a–c and Table 1). Based on IUPAC classification, the N_2 uptake isotherms were type III for TPA-BBT-CMP, type II for Py-BBT-CMP, and type II and IV for TPE-BBT-CMP. Both N_2 profiles of the Py-BBT-CMP and TPE-BBT-CMP showed rapid N_2 uptake at a low and high relative pressure (P/P_0), indicating the presence of micro- and mesoporosity properties within these two materials. The specific surface area and total pore volumes of TPA-BBT-CMP, Py-BBT-CMP, and TPE-BBT-CMP were found to be $35.6 \text{ m}^2 \text{ g}^{-1}$ and $0.16 \text{ cm}^3 \text{ g}^{-1}$, $67 \text{ m}^2 \text{ g}^{-1}$ and $0.024 \text{ cm}^3 \text{ g}^{-1}$, and $410 \text{ m}^2 \text{ g}^{-1}$ and $0.50 \text{ cm}^3 \text{ g}^{-1}$, respectively. Finally, the pore size diameters of TPA-BBT-CMP, Py-BBT-CMP, and TPE-BBT-CMP were 2.7, 1.3, and 1.8 nm, respectively (based on nonlocal density functional theory (NL-DFT)) (Figure 2d–f).

The surface morphological of TPA-BBT-CMP, Py-BBT-CMP, and TPE-BBT-CMP featured irregular aggregated sphere, rod, and regular sphere aggregate structures, respectively, as displayed in SEM images (Figure 3A(a1–a3)). Furthermore, TEM images of all BBT-CMPs are shown in Figure 3B(b1–b3), which revealed the presence of small pores and the presence of dark and bright areas in their structure, confirming their non-order and amorphous nature.

2.3. Electrochemical Performance of BBT-CMPs

The electrochemical performance of BBT-CMP samples was evaluated using cyclic voltammetry (CV) and galvanostatic charge–discharge (GCD) analyses using glassy carbon (as the working electrode), Hg/HgO (as reference electrode), and platinum wire (as a counter electrode) in 1 M KOH aqueous solution. Figure 4a–c display the corresponding CV curves of BBT-CMP samples at different scan rates from 5 to 200 mV s^{-1} , recorded within the potential window of 0.00 to -1.00 V (vs. Hg/HgO). The synergism of ELDC and PC can be confirmed from the rectangle-shaped, humped CV curves of all the BBT-CMPs, even at a high scan rate of 200 mV s^{-1} [2,12,19]. The CV curves of all the BBT-CMPs exhibit

a little deviation from the capacitive nature due to the pseudocapacitive effect [69,70], which is the result of fast redox reactions occurring on and near the surface of active materials during charge and discharge [69,71]. As shown in Figure 4a–c, the presence of a hump/spike indicates the contribution of pseudocapacitance, which arose from the presence of various types of nitrogen and sulfur heteroatoms that enable easier accessibility of electrolytes to the electrode surface and transfer of electrons [72,73]. The Py–BBT–CMP sample showed a higher integrated area than the other two samples (TPA– and TPE–BBT–CMP), which reveals its superior electrochemical performance. Furthermore, increasing the sweep rate from 5 to 200 mV s^{-1} enhanced the current density while maintaining the form of the CV curves, suggesting strong rate capability and simple kinetics. Figure 4d–f represent the GCD curves of the BBT–CMP samples, recorded within the potential window of 0.00 to -1.00 V (vs. Hg/HgO) at various current densities from 0.5 to 20 A g^{-1} . The GCD curves of all BBT–CMP samples displayed triangular forms with a small bend, suggesting that the presence of distinct kinds of N and S heteroatoms caused both EDLC features and pseudocapacitance [2,12,14]. The discharging times of the Py–BBT–CMP (455.6 sec at 0.5 A g^{-1}) sample was longer than that of both TPA–BBT–CMP (439 s at 0.5 A g^{-1}) and TPE–BBT–CMP (426.6 s at 0.5 A g^{-1}) samples (Figure 4d–f).

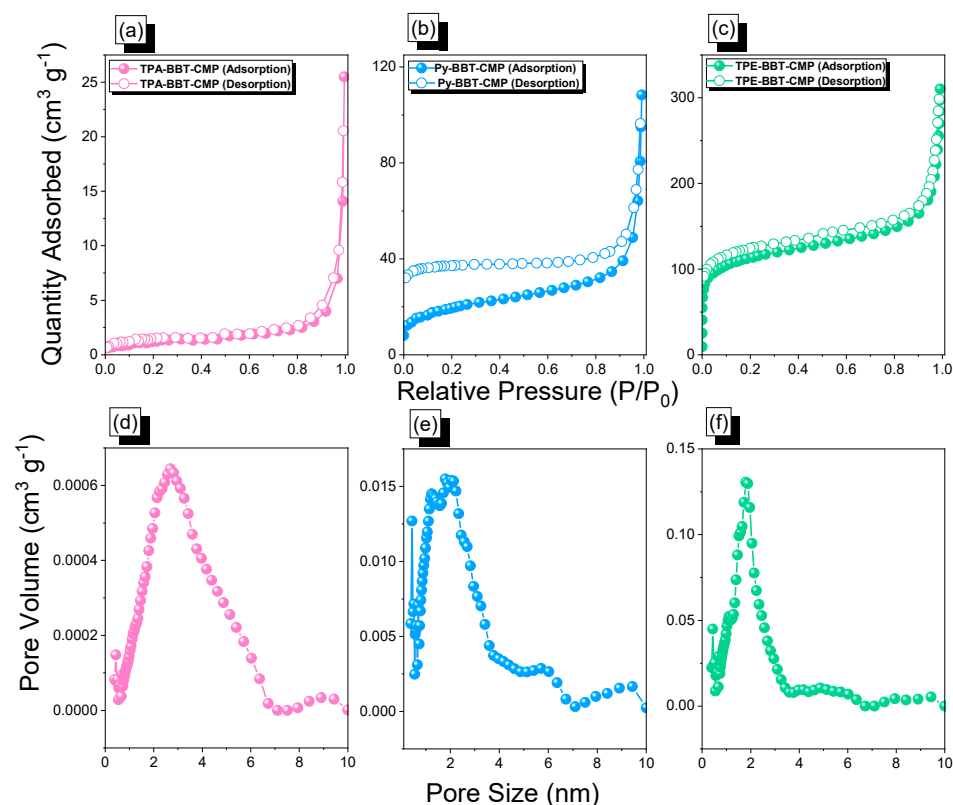


Figure 2. N_2 Uptake and pore size diameter curves of the TPA–BBT–CMP (a,d), Py–BBT–CMP (b,e), and TPE–BBT–CMP (c,f).

Figure 5a shows the specific capacitances of all BBT–CMP samples determined from GCD curves using Equation (1).

$$C_s = (I\Delta t)/(m\Delta V) \quad (1)$$

where C_s (F g^{-1}) is the specific capacitance of the supercapacitor, I (A) is the discharge current, ΔV (V) is the potential window, Δt (s) is the discharge time, and m (g) is the mass of the NPC on the electrode.

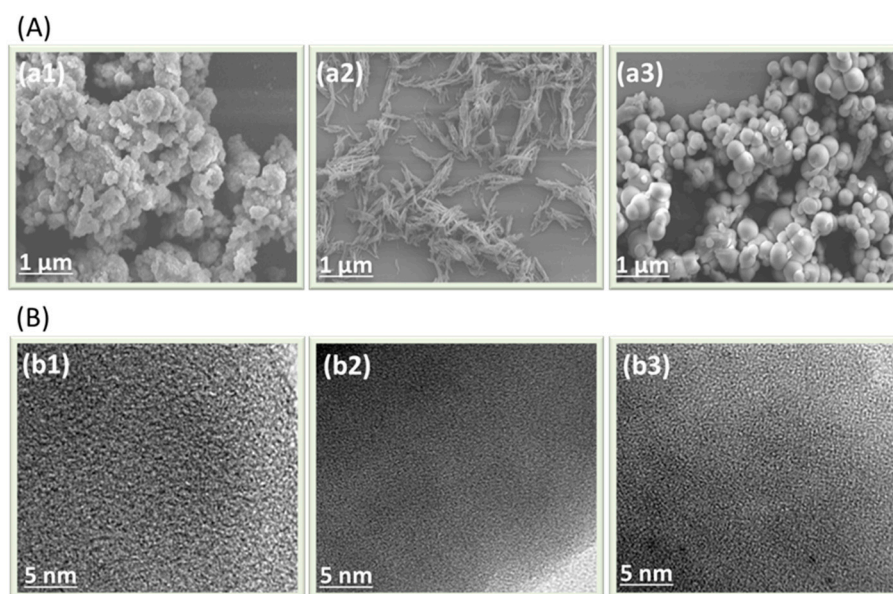


Figure 3. (A) SEM and (B) TEM images of the TPA-BBT-CMP (a1,b1), Py-BBT-CMP (a2,b2), and TPE-BBT-CMP (a3,b3).

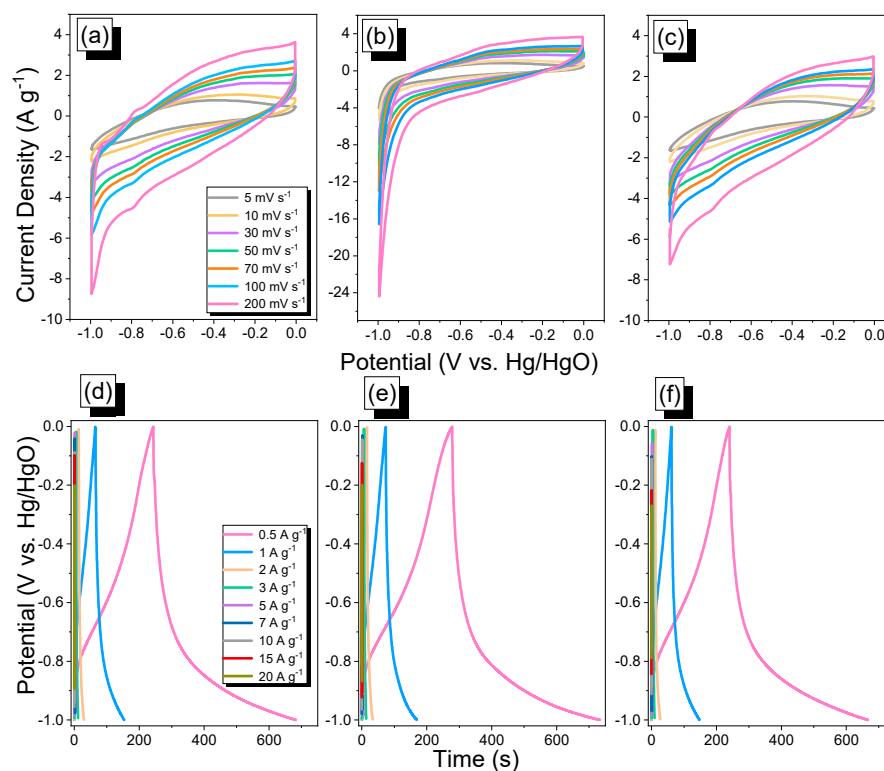


Figure 4. CV and GCD analyses of the TPA-BBT-CMP (a,d), Py-BBT-CMP (b,e), and TPE-BBT-CMP (c,f).

All BBT-CMP samples displayed superior capacitance (TPA-BBT-CMP, 220 F g^{-1} ; Py-BBT-CMP, 228 F g^{-1} ; TPE-BBT-CMP, 214 F g^{-1} , at 0.5 A g^{-1}), compared with other porous materials (Table S2). This behavior could be explained by the presence of various types of N and S heteroatoms, which enable easier accessibility of electrolytes to the electrode surface. In addition, upon increasing the current density from 0.5 to 20 A g^{-1} , the specific capacitances of all BBT-CMP samples decreased due to the insufficient time available for ion diffusion at high current densities. Our lab has recently made two ferrocene-derived conjugated

microporous polymers (FFC-CMPs) via Sonogashira couplings [12], and these materials showed low values of specific capacitances at 0.5 A g^{-1} (Table S2). In addition, we prepared three CMPs (TBN-TPE-CMP, TBN-Py-CMP, TBN-Car-CMP) via Sonogashira-Hagihara cross-couplings [19]. The electrochemical performance of the three TBN-CMP samples revealed specific capacitances in the range 18.45, 31, and 18.90 F g^{-1} . Moreover, we prepared two-hybrid porous polymers (POIPs) through the Heck reaction of octavinylsilsesquioxane with brominated fluorene and anthraquinone (A-Br_2) with octavinylsilsesquioxane (OVS) [10]. We revealed that POSS (polyhedral oligomeric silsesquioxane)-A-POIP had higher capacitance than POSS-F-POIP due to the π -conjugated system and faradaic reaction of the anthraquinone unit. The durability of all samples was tested through GCD measurements over 2000 cycles at a current density of 10 A g^{-1} (Figure 5b). The TPA-BBT-CMP, Py-BBT-CMP, and TPE-BBT-CMP samples displayed good cycling stability (Figures 5b and S18), with 91.8%, 93.2%, and 99.5% retention, respectively, of their original capacitances after 2000 cycles, indicating their excellent cycling stability in 1 M KOH as the electrolyte. Energy (E , Wh kg^{-1}) and power densities (P , W kg^{-1}) were calculated using Equations (2) and (3), respectively, to build the Ragone plot.

$$E = 1000C(\Delta V)^2 / (2 \times 3600) \quad (2)$$

$$P = E / (t/3600) \quad (3)$$

The Ragone plot (Figure 5c) showed that the energy and power densities of the Py-BBT-CMP sample were higher than those of the TPA-BBT-CMP and TPE-BBT-CMP samples, suggesting that the Py-BBT-CMP sample possessed good energy and power densities.

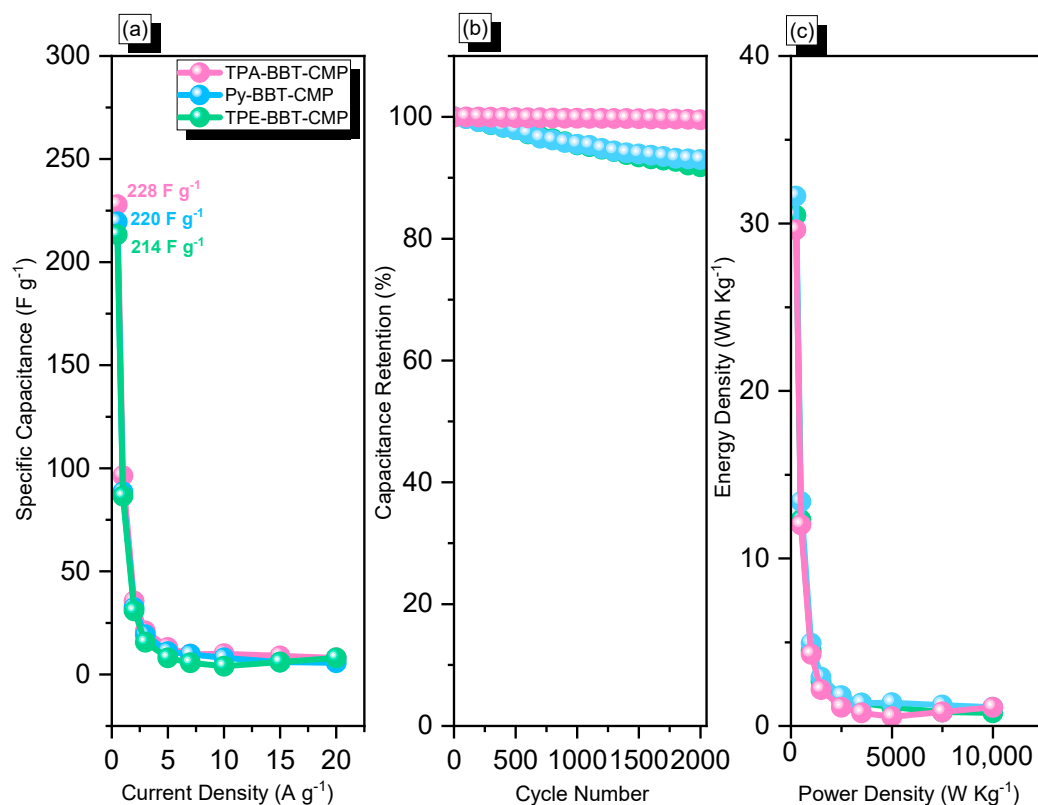


Figure 5. Capacitance (a), stability (b), and Ragone plots (c) of TPA-BBT-CMP, Py-BBT-CMP, and TPE-BBT-CMP.

We investigated the electronic structure of the monomers and polymers using density functional theory (DFT) to gain a better understanding of the three BBT-CMP polymers' superior electrochemical performance. The charge storage ability and redox characteristics

of CMPs are influenced by their electronic structure. The basis set 6–31G was employed using the hybrid functional B3LYP (d). To accommodate for long-range and noncovalent interactions, we employed the D3BJ dispersion correction. For the ground state geometry of the monomers, we investigated many conformers and chose the one with the lowest energy. The global minimum was then confirmed using harmonic vibrational frequency. At the same level of theory, the highest occupied molecular orbital (HOMO) and lowest unoccupied molecular orbital (LUMO) energy gaps, as well as the molecular electrostatic potential (MESP), were calculated on the optimized geometries. The LUMO distribution has a significant influence on the polymer's electrochemical performance. The high delocalization degree of LUMO orbitals endows the BBT–CMP polymers with high n-doping activity. Moreover, the narrow bandgap of the BBT–CMP polymers (Figure 6) leads to a higher electron conductivity and, as a result, superior electrochemical performance.

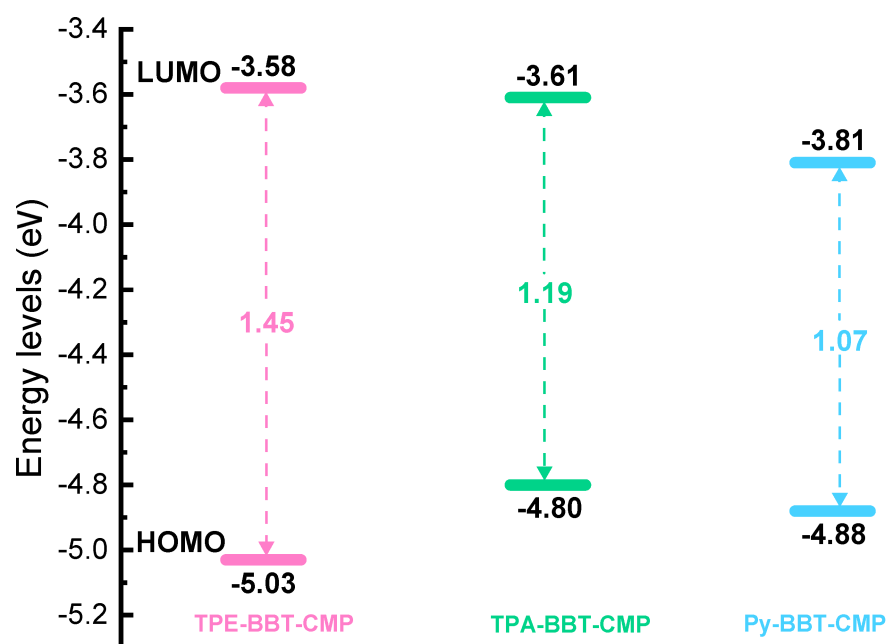


Figure 6. HOMO–LUMO diagrams for TPE–BBT–CMP, TPA–BBT–CMP, and Py–BBT–CMP.

Figures 7 and S19 presented the frontier molecular orbitals of the building blocks monomers (BBT, TPE, TPA, Py, and TPE) and the synthesized three BBT–CMPs. Both HOMO and LUMO are highly delocalized and are spread all over the whole molecule for the building blocks monomers and BBT–CMP polymers, as shown in Figure 7a–c and Figure S19, respectively. Figure 7d–f depict the molecular electrostatic potential (MESP) analysis of TPE–BBT–CMP, TPA–BBT–CMP, and Py–BBT–CMP samples. Figure S20 presents the molecular electrostatic potential (MESP) analysis of the building blocks monomers (TPE, TPA, Py, and BBT). The high delocalization leads to decreasing the charge density over active sites. Low negative charge density at redox-active sites (N in all polymers) may impair their contact with the electrolyte, allowing for quicker ion diffusion and electron transfer through CMP pores. The prolonged conjugation in all three polymers leads to improved electron conduction, a highly delocalized LUMO distribution, tiny band gaps, and lower negative charge density on redox-active sites. These characteristics boost the electrochemical performance of these polymers.

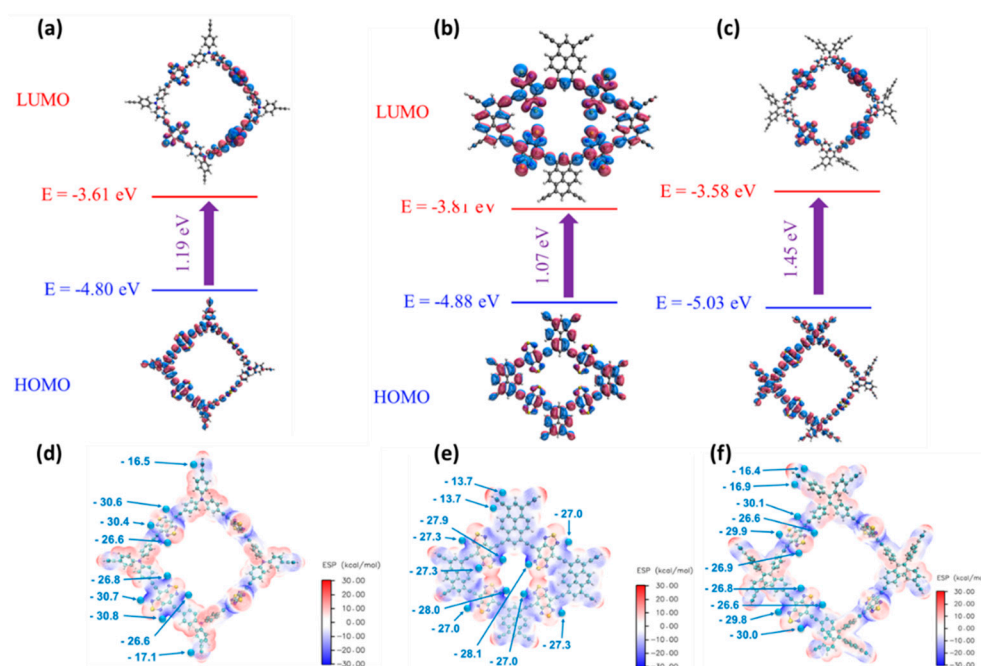


Figure 7. Energy levels and MESP diagrams of the TPA-BBT-CMP (a,d), Py-BBT-CMP (b,e), and TPE-BBT-CMP (c,f).

3. Synthesis Methods

3.1. Materials

N,N-dimethylformamide (DMF, 99.9%), thionyl chloride (SOCl_2 , 99%), bromine solution (Br_2 , 99.5%), triphenylamine (TPA, 98%), hydrobromic acid (HBr, 48%), benzophenone (99%), triethylamine (Et_3N , 99.5%), dichloromethane (DCM), methanol (MeOH), tetrahydrofuran (THF), acetone, hydrochloric acid solution (HCl, 12 M), $\text{Pd}(\text{PPh}_3)_4$ (99%), and sodium carbonate (NaCO_3 , 99.5%) were purchased commercially from Alfa Aesar (Lancashire, UK), Acros (Fukuoka, Japan), and Sigma-Aldrich (Burlington, MA, USA). 1,3,6,8-tetraethynylpyrene (Py-T), and 1,1,2-tetrakis(4-ethynylphenyl)ethene (TPE-T) were synthesized according to previously reported procedures [19,41].

3.2. Synthesis of 4,7-Dibromobenzo[*c*][1,2,5]thiadiazole (BT- Br_2)

BT (10.0 g, 73.4 mmol), 80 mL of HBr (48%), and (35.2 g, 220.3 mmol) of Br_2 solution were mixed, and the mixture was refluxed at 95 °C for 9 h. Then, the mixture solution was added into NaOH solution at 0 °C, and the total solution was worked up by using DCM to afford a BT- Br_2 as a white powder (5 g, 50%). FTIR (Figure S1): 3035. ^1H NMR (Figure S2): 7.73 ppm. ^{13}C NMR (Figure S3): 153.5, 133, 114.50 ppm.

3.3. Synthesis of 4,7-Dibromo-5,6-dinitrobenzo[*c*][1,2,5]thiadiazole (BT-2 NO_2)

BT-2 NO_2 was synthesized via the nitration of BT- Br_2 (2 g, 6.8 mmol) with 28 mL of conc. H_2SO_4 and 14 mL of fuming HNO_3 at 0 °C, and the solution was refluxed up to 90 °C for 24 h. Then, the mixture solution was added into Na_2CO_3 solution at 0 °C to provide a white crystal (1.30 g, 65%). FTIR (Figure S4): 1343 cm^{-1} (NO_2 group). ^1H NMR (Figure S5): no signal observed. (+) ESI-MS (Figure S6): 381.10. $T_{d10} = 256$ °C (Figure S7).

3.4. Synthesis of 4,7-Dibromobenzo[*c*][1,2,5]thiadiazole-5,6-diamine (BT-2 NH_2)

BT-2 NH_2 was synthesized via the reduction reaction of BT-2 NO_2 (500 mg, 1.3 mmol) in 20 mL of acetic solution in the presence of Fe (0.875 mg, 15.67 mmol) at room temperature and acetic acid (10 mL). The mixture solution was added into ice water to obtain yellow powder (400 mg, 80%). FTIR (Figure S8): 3323, 3290 cm^{-1} (NH_2 group). ^1H

NMR (Figure S9): 4.52 ppm (4H, 2NH₂). (+) ESI-MS (Figure S10): 322.90. T_{d10} = 228 °C (Figure S11).

3.5. Synthesis of 4,8-Dibromobenzo(1,2-*c*;4,5-*c'*)bis(1,2,5)thiadiazole (BBT-Br₂)

In 100 mL of three necks under N₂ environment, BT-2NH₂ (500 mg, 1.54 mmol) was degassed twice a time under vacuum; then, DCM (10 mL), triethylamine (860 µL, 6.17 mmol), and thionyl chloride (220 µL, 3.1 mmol) were added at 0 °C. Afterward, the mixture was stirred and heated for 12 h at 50 °C, and DCM was removed using rotary evaporation; then, the mixture was added to 3N HCl and stirred for 30 min. Finally, it was filtered and washed using MeOH and reprecipitated by DCM and MeOH; thus, a dark red powder was obtained (368 mg, 68%). FTIR (Figure S12): 3050, 1611 cm⁻¹ (NH₂ group). ¹H NMR (Figure S13): no signal observed. (+) ESI-MS (Figure S14): 353. T_{d10} (thermal decomposition temperatures at 10% weight loss) = 262 °C (Figure S15).

3.6. Synthesis of Tris(4-((trimethylsilyl)ethynyl)phenyl)amine (TPA-TMS)

Pd(PPh₃)₄ (0.150 mmol), PPh₃ (0.470 mmol), CuI (0.310 mmol), and TPA-Br₃ (2.07 mmol) were mixed in THF (50 mL). Trimethylsilyl acetylene (1.42 g, 15.5 mmol) was added, and the mixture was refluxed for 3 days. After cooling, the contents inside the flask were endowed for cooling and then filtered off and extracted with DCM (50 mL); then, the solvent was evaporated, and the pure TPA-TMS as a yellow solid (900 mg, 90%) was obtained after running column chromatography (Scheme S1). FTIR (Figure S16a) 3035, 2109 (C≡C stretching) cm⁻¹. ¹H NMR (Figure S17a): 7.34 (s, 6H), 6.97 (s, 6H), 0.257 (s, 27H, CH₃) ppm. ¹³C NMR (Figure S17c): 148.14, 134.03, 124.83, 118.49, 105.83, 93.83, 0.09 ppm.

3.7. Synthesis of Tris(4-ethynylphenyl)amine (TPA-T)

TPA-TMS (0.520 g, 0.970 mmol) and K₂CO₃ (1.00 g, 7.24 mmol) were stirred in MeOH (25 mL) at 27 °C for 1 d. The solvent was evaporated and added to H₂O (100 mL) to yield TPA-T (450 mg, 87%, Scheme S1). FTIR (Figure S16b): 3276 (≡C-H), 2109 (C≡C stretching) cm⁻¹. ¹H NMR (Figure S17b): 7.39 (s, 6H), 7.03 (s, 6H), 3.04 (s, 3H) ppm. ¹³C NMR (Figure S17d): 148.48, 134.03, 124.15, 117.8, 83.28 ppm.

3.8. Synthesis of BBT-CMP Materials

In the Schlenk storage tube, 0.1 g of TPA-Br₃ or 0.1 g of Py-Br₄ or 0.1 g of TPE-Br₄ was dissolved in the presence of CuI, PPh₃, Pd(PPh₃)₄, and BBT-Br₂ in a mixture of DMF and Et₃N. Further, the tube was stirred and heated for 72 h at 100 °C. The obtained product was washed with different organic solvents such as DMF, THF, and acetone. The product was dried at 70 °C to obtain brown powder for TPA-BBT-CMP (0.08 g, 80%, Scheme 2e); reddish-brown powder for Py-BBT-CMP (0.09 g, 90%, Scheme 2f); orange powder for TPE-BBT-CMP (0.07 g, 70%, Scheme 2g).

4. Characterization

FTIR spectra were recorded using a Bruker Tensor 27 FTIR spectrophotometer with a resolution of 4 cm⁻¹ through the KBr disk method. ¹³C Nuclear magnetic resonance (NMR) spectra were recorded using an INOVA 500 instrument with DMSO-*d*₆ as the solvent and TMS as the external standard; chemical shifts are reported in parts per million (ppm). The thermal stabilities of the samples were examined under a N₂ atmosphere using a TG Q-50 thermogravimetric analyzer; each cured sample (ca. 5 mg) was placed in a Pt cell and heated at a rate of 20 °C min⁻¹ from 100 to 800 °C under a N₂ flow rate of 60 mL min⁻¹. Wide-angle X-ray diffraction (WAXD) patterns were measured using the wiggler beam-line BL17A1 of the National Synchrotron Radiation Research Center (NSRRC), Taiwan; a triangular bent Si (111) single crystal was used to give a monochromated beam having a wavelength (λ) of 1.33 Å. The morphologies of the polymer samples were examined using field emission scanning electron microscopy (FE-SEM; JEOL JSM7610F) and transmission electron microscopy (TEM), using a JEOL-2100 instrument operated at an accelerating

voltage of 200 kV. The Brunauer–Emmett–Teller (BET) surface areas and porosities of the samples (ca. 40–100 mg) were measured using BEL MasterTM/BEL simTM (v. 3.0.0). N₂ adsorption and desorption isotherms were generated through incremental exposure to ultrahigh purity N₂ (up to ca. 1 atm) in a liquid N₂ (77 K) bath. Surface parameters were calculated using the BET adsorption models in the instrument's software. The pore sizes of the prepared samples were determined using nonlocal density functional theory (NLDFT).

5. Conclusions

In conclusion, three types of CMPs (TPA–BBT, Py–BBT, and TPE–BBT–CMPs) based on BBT unit were successfully synthesized via Sonogashira coupling's reaction, for application as electrode materials in energy storage systems. Several techniques were employed to characterize the porosity, thermal stability, and morphologies of the new BBT–CMP properties such as BET, TGA, SEM, and TEM. More interestingly, TPA–BBT–CMP, Py–BBT–CMP, and TPE–BBT–CMP electrodes featured high specific capacitance values of 220, 228, and 214 F g^{−1}, respectively, at a current of 0.5 A g^{−1}, and they could retain their durability up to after 2000 cycles at a current of 10 A g^{−1}, due to their highly delocalized LUMO distribution and highly delocalized LUMO distribution and small bandgaps (based on DFT and MESP analyses). The unique properties of BBT–CMPs, as shown above, make them ideal candidates for energy storage and other potential applications.

Supplementary Materials: The following supporting information can be downloaded at: <https://www.mdpi.com/article/10.3390/molecules27062025/s1>, Scheme S1: Syntheses of (a) TPA–TMS and (b) TPA–T, Figure S1: FTIR spectrum of BT–Br₂, Figure S2: ¹H-NMR spectrum of BT–Br₂, Figure S3: ¹³C-NMR spectrum of BT–Br₂, Figure S4: FTIR spectrum of BT–2NO₂, Figure S5: ¹H-NMR spectrum of BT–2NO₂, Figure S6: (+) ESI-MS spectrum of BT–2NO₂, Figure S7: TGA profile of BT–2NO₂, Figure S8: ¹H-NMR spectrum of BT–2NH₂, Figure S9: ¹H-NMR spectrum of BT–2NH₂, Figure S10'' (+) ESI-MS spectrum of BT–2NH₂, Figure S11: TGA profile of BT–2NH₂, Figure S12: ¹H-NMR spectrum of BBT–Br₂, Figure S13: ¹H-NMR spectrum of BBT–Br₂, Figure S14: (+) ESI-MS spectrum of BBT–Br₂, Figure S15: TGA profile of BBT–Br₂, Figure S16: FTIR spectra of (a) TPA–TMS and (b) TPA–T, Figure S17: (a,b) ¹H and (c,d) ¹³C NMR spectra of (a,c) TPA–TMS and (b,d) TPA–T, Figure S18: Stability performance of (a) TPA–BBT–CMP, (b) Py–BBT–CMP, and (c) TPE–BBT–CMP after 2000 cycles, Figure S19: Energy level profiles of (a) BBT, (b) TPA, (c) Py, and (d) TPE compounds, Figure S20: The molecular electrostatic potential of (a) BBT, (b) TPA, (c) Py and (d) TPE, Table S1: Summarized the thermal stability of BT–2NO₂, BT–2NH₂, BBT–Br₂, TPA–BBT–CMP, Py–BBT–CMP, and TPE–BBT–CMP, Table S2: Comparison between the specific surface area/specific capacitance of BBT–CMP samples with those of previously reported materials for supercapacitor application [2,10,12,13,19,33,73–76].

Author Contributions: Conceptualization, M.G.M., T.H.M., M.M.S., A.A.K.M. and Y.T.; methodology, M.G.M., T.H.M. and M.M.S.; software, A.A.K.M.; validation, M.G.M., T.H.M., M.M.S., T.A., S.M.A., J.K. and B.M.M.; formal analysis, M.G.M., T.H.M., M.M.S., A.A.K.M. and Y.T.; investigation, M.G.M., T.H.M., M.M.S., A.A.K.M. and Y.T.; resources, S.-W.K.; data curation, M.G.M., T.H.M., M.M.S. and A.A.K.M.; writing—original draft preparation, M.G.M., T.H.M., M.M.S., A.A.K.M., K.C.-W.W. and S.-W.K.; writing—review and editing, M.G.M., T.H.M., M.M.S., A.A.K.M. and S.-W.K.; visualization, M.G.M., T.H.M., M.M.S., A.A.K.M. and S.-W.K.; supervision, K.C.-W.W. and S.-W.K.; project administration, M.G.M., K.C.-W.W. and S.-W.K.; funding acquisition, K.C.-W.W. and S.-W.K. All authors have read and agreed to the published version of the manuscript.

Funding: This study was supported financially by the Ministry of Science and Technology, Taiwan, under contracts MOST 106-2221-E-110-067-MY3, 108-2638-E-002-003-MY2, and 108-2221-E-110-014-MY3.

Institutional Review Board Statement: Not applicable.

Informed Consent Statement: Not applicable.

Data Availability Statement: The data presented in this study are available in the article and supplementary material.

Acknowledgments: This study was supported financially by the Ministry of Science and Technology, Taiwan, under contracts MOST 108-2221-E-110-014-MY3. The authors (T.A. and S.M.A.) thank the Researchers Supporting Project Number (RSP-2021/29), King Saud University, Riyadh, Saudi Arabia. The authors thank the staff at National Sun Yat-sen University for their assistance with TEM (ID: EM022600) experiments. The authors acknowledge a generous allocation of computer time granted by Compute Canada's national HPC platform.

Conflicts of Interest: The authors declare no conflict of interest.

Sample Availability: Samples of the compounds are not available from the authors.

References

1. Lin, Z.; Goikolea, E.; Balducci, A.; Naoi, K.; Taberna, P.L.; Salanne, M.; Yushin, G.; Simon, P. Materials for supercapacitors: When Li-ion battery power is not enough. *Mater. Today* **2018**, *21*, 419–436. [[CrossRef](#)]
2. Mohamed, M.G.; Samy, M.M.; Mansoure, T.H.; Li, C.-J.; Li, W.-C.; Chen, J.-H.; Zhang, K.; Kuo, S.-W. Microporous Carbon and Carbon/Metal Composite Materials Derived from Bio-Benzoxazine-Linked Precursor for CO₂ Capture and Energy Storage Applications. *Int. J. Mol. Sci.* **2022**, *23*, 347. [[CrossRef](#)]
3. Kang, C.W.; Ko, Y.-J.; Lee, S.M.; Kim, H.J.; Choi, J.; Son, S.U. Carbon black nanoparticle trapping: A strategy to realize the true energy storage potential of redox-active conjugated microporous polymers. *J. Mater. Chem. A* **2021**, *9*, 17978–17984. [[CrossRef](#)]
4. Shi, R.; Han, C.; Duan, H.; Xu, L.; Zhou, D.; Li, H.; Li, J.; Kang, F.; Li, B.; Wang, G. Redox-Active Organic Sodium Anthraquinone-2-Sulfonate (AQS) Anchored on Reduced Graphene Oxide for High-Performance Supercapacitors. *Adv. Energy Mater.* **2018**, *8*, 1802088. [[CrossRef](#)]
5. Septiani, N.L.W.; Kaneti, Y.V.; Fathoni, K.B.; Wang, J.; Ide, Y.; Yulianto, B.; Nugraha; Dipojono, H.K.; Nanjundan, A.K.; Golberg, D.; et al. Self-assembly of nickel phosphate-based nanotubes into two-dimensional crumpled sheet-like architectures for high-performance asymmetric supercapacitors. *Nano Energy* **2020**, *67*, 104270. [[CrossRef](#)]
6. Wang, Y.; Li, W.; Zhang, L.; Zhang, X.; Tan, B.; Hao, J.; Zhang, J.; Wang, X.; Hu, Q.; Lu, X. Amorphous cobalt hydrogen phosphate nanosheets with remarkable electrochemical performances as advanced electrode for supercapacitors. *J. Power Sources* **2020**, *449*, 227487. [[CrossRef](#)]
7. Mohamed, M.G.; Samy, M.M.; Mansoure, T.H.; Sharma, S.U.; Tsai, M.-S.; Chen, J.-H.; Lee, J.-T.; Kuo, S.-W. Dispersions of 1,3,4-Oxadiazole-Linked Conjugated Microporous Polymers with Carbon Nanotubes as a High-Performance Electrode for Supercapacitors. *ACS Appl. Energy Mater.* **2022**. [[CrossRef](#)]
8. Mei, L.; Cui, X.; Duan, Q.; Li, Y.; Lv, X.; Wang, H.-G. Metal phthalocyanine-linked conjugated microporous polymer hybridized with carbon nanotubes as a high-performance flexible electrode for supercapacitors. *Int. J. Hydrogen Energy* **2020**, *45*, 22950–22958. [[CrossRef](#)]
9. El-Mahdy, A.F.M.; Yu, T.C.; Mohamed, M.G.; Kuo, S.-W. Secondary Structures of Polypeptide-Based Diblock Copolymers Influence the Microphase Separation of Templates for the Fabrication of Microporous Carbons. *Macromolecules* **2020**, *54*, 1030–1042. [[CrossRef](#)]
10. Mohamed, M.G.; Mansoure, T.H.; Takashi, Y.; Samy, M.M.; Chen, T.; Kuo, S.-W. Ultrastable porous organic/inorganic polymers based on polyhedral oligomeric silsesquioxane (POSS) hybrids exhibiting high performance for thermal property and energy storage. *Microporous Mesoporous Mater.* **2021**, *328*, 111505. [[CrossRef](#)]
11. El-Mahdy, A.F.M.; Liu, T.-E.; Kuo, S.-W. Direct synthesis of nitrogen-doped mesoporous carbons from triazine-functionalized resol for CO₂ uptake and highly efficient removal of dyes. *J. Hazard. Mater.* **2020**, *391*, 122163. [[CrossRef](#)] [[PubMed](#)]
12. Samy, M.M.; Mohamed, M.G.; Mansoure, T.H.; Meng, T.S.; Khan, M.A.R.; Liaw, C.-C.; Kuo, S.-W. Solid state chemical transformations through ring-opening polymerization of ferrocene-based conjugated microporous polymers in host–guest complexes with benzoxazine-linked cyclodextrin. *J. Taiwan Inst. Chem. Eng.* **2022**, *132*, 104110. [[CrossRef](#)]
13. Samy, M.M.; Mohamed, M.G.; Kuo, S.-W. Pyrene-functionalized tetraphenylethylene polybenzoxazine for dispersing single-walled carbon nanotubes and energy storage. *Compos. Sci. Technol.* **2020**, *199*, 108360. [[CrossRef](#)]
14. Abuzeid, H.R.; El-Mahdy, A.F.M.; Kuo, S.-W. Covalent organic frameworks: Design principles, synthetic strategies, and diverse applications. *Giant* **2021**, *6*, 100054. [[CrossRef](#)]
15. Luo, B.C.; Chen, Y.; Zhang, Y.B.; Huo, J.Q. Nitrogen-rich anthraquinone–triazine conjugated microporous polymer networks as high-performance supercapacitor. *New J. Chem.* **2021**, *45*, 17278–17286. [[CrossRef](#)]
16. Mohamed, M.G.; Sharma, S.U.; Liu, N.Y.; Mansoure, T.H.; Samy, M.M.; Chaganti, S.V.; Chang, Y.C.; Lee, J.T.; Kuo, S.-W. Ultrastable Covalent Triazine Organic Framework Based on Anthracene Moiety as Platform for High-Performance Carbon Dioxide Adsorption and Supercapacitors. *Int. J. Mol. Sci.* **2022**, *23*, 3174. [[CrossRef](#)]
17. Mohamed, M.G.; El-Mahdy, A.F.M.; Kotp, M.G.; Kuo, S.-W. Advances in porous organic polymers: Syntheses, structures, and diverse applications. *Mater. Adv.* **2022**, *3*, 707–733. [[CrossRef](#)]
18. Mohamed, M.G.; Atayde, E.C.; Matsagar, B.M.; Na, J.; Yamauchi, Y.; Wu, K.C.-W.; Kuo, S.-W. Construction Hierarchically Mesoporous/Microporous Materials Based on Block Copolymer and Covalent Organic Framework. *J. Taiwan Inst. Chem. Eng.* **2020**, *112*, 180–192. [[CrossRef](#)]

19. Samy, M.M.; Mohamed, M.G.; El-Mahdy, A.F.M.; Mansoure, T.H.; Wu, K.C.-W.; Kuo, S.-W. High-performance supercapacitor electrodes prepared from dispersions of tetrabenzonaphthalene-based conjugated microporous polymers and carbon nanotubes. *ACS Appl. Mater. Interfaces* **2021**, *13*, 51906–51916. [[CrossRef](#)]
20. Mohamed, M.G.; Ahmed, M.M.M.; Du, W.-T.; Kuo, S.-W. Meso/Microporous Carbons from Conjugated Hyper-Crosslinked Polymers Based on Tetraphenylethene for High-Performance CO₂ Capture and Supercapacitor. *Molecules* **2021**, *26*, 738. [[CrossRef](#)]
21. El-Mahdy, A.F.M.; Yu, T.C.; Kuo, S.-W. Synthesis of multiple heteroatom-doped mesoporous carbon/silica composites for supercapacitors. *Chem. Eng. J.* **2021**, *414*, 128796. [[CrossRef](#)]
22. Aziz, S.B.; Nofal, M.M.; Abdulwahid, R.T.; Kadir, M.F.Z.; Hadi, J.M.; Hessien, M.M.; Kareem, W.O.; Dannoun, E.M.A.; Saeed, S.R. Impedance, FTIR and transport properties of plasticized proton conducting biopolymer electrolyte based on chitosan for electrochemical device application. *Results Phys.* **2021**, *29*, 104770. [[CrossRef](#)]
23. Gaida, B.; Brzeczek-Szafran, A. Insights into the Properties and Potential Applications of Renewable Carbohydrate-Based Ionic Liquids: A Review. *Molecules* **2020**, *25*, 3285. [[CrossRef](#)]
24. Aziz, S.B.; Abdulwahid, R.T.; Kadir, M.F.Z.; Ghareeb, H.O.; Ahamad, T.; Alshehri, S.M. Design of non-faradaic EDLC from plasticized MC based polymer electrolyte with an energy density close to lead-acid batteries. *J. Ind. Eng. Chem.* **2022**, *105*, 414–426. [[CrossRef](#)]
25. Aziz, S.B.; Dannoun, E.M.A.; Abdulwahid, R.T.; Kadir, M.F.Z.; Nofal, M.M.; Al-Saeedi, S.I.; Murad, A.R. The Study of Ion Transport Parameters in MC-Based Electrolyte Membranes Using EIS and Their Applications for EDLC Devices. *Membranes* **2022**, *12*, 139. [[CrossRef](#)] [[PubMed](#)]
26. Mohamed, M.G.; Tsai, M.-Y.; Wang, C.-F.; Huang, C.-F.; Danko, M.; Dai, L.; Chen, T.; Kuo, S.-W. Multifunctional Polyhedral Oligomeric Silsesquioxane (POSS) Based Hybrid Porous Materials for CO₂ Uptake and Iodine Adsorption. *Polymers* **2021**, *13*, 221. [[CrossRef](#)]
27. He, Y.; Cheng, Z.H.; Zuo, H.Y.; Yan, C.N.; Liao, Y.Z. Green Synthesis of Pyridyl Conjugated Microporous Polymers as Precursors for Porous Carbon Microspheres for Efficient Electrochemical Energy Storage. *ChemElectroChem* **2019**, *7*, 959–966. [[CrossRef](#)]
28. Mohamed, M.G.; Lee, C.-C.; El-Mahdy, A.F.M.; Lüder, J.; Yu, M.-H.; Li, Z.; Zhu, Z.; Chueh, C.-C.; Kuo, S.-W. Exploitation of two-dimensional conjugated covalent organic frameworks based on tetraphenylethylene with bicarbazole and pyrene units and applications in perovskite solar cells. *J. Mater. Chem. A* **2020**, *8*, 11448–11459. [[CrossRef](#)]
29. Zhang, C.; He, Y.; Mu, P.; Wang, X.; He, Q.; Chen, Y.; Zeng, J.; Wang, F.; Xu, Y.; Jiang, J.-X. Toward High Performance Thiophene-Containing Conjugated Microporous Polymer Anodes for Lithium-Ion Batteries through Structure Design. *Adv. Funct. Mater.* **2018**, *28*, 1705432. [[CrossRef](#)]
30. Zhang, T.; Xing, G.; Chen, W.; Chen, L. Porous organic polymers: A promising platform for efficient photocatalysis. *Mater. Chem. Front.* **2019**, *4*, 332–353. [[CrossRef](#)]
31. Elewa, A.M.; El-Mahdy, A.F.; Elsayed, M.H.; Mohamed, M.G.; Kuo, S.-W.; Chou, H.-H. Sulfur-doped Triazine-Conjugated Microporous Polymers for Achieving the Robust Visible-light-driven Hydrogen Evolution. *Chem. Eng. J.* **2021**, *421*, 129825. [[CrossRef](#)]
32. Amin, K.; Ashraf, N.; Mao, L.; Faul, C.F.; Wei, Z. Conjugated microporous polymers for energy storage: Recent progress and challenges. *Nano Energy* **2021**, *85*, 105958. [[CrossRef](#)]
33. Mohamed, M.G.; Chen, T.-C.; Kuo, S.-W. Solid-State Chemical Transformations to Enhance Gas Capture in Benzoxazine-Linked Conjugated Microporous Polymers. *Macromolecules* **2021**, *54*, 5866–5877. [[CrossRef](#)]
34. Park, S.Y.; Kang, C.W.; Lee, S.M.; Kim, H.J.; Ko, Y.; Choi, J.; Son, S.U. Nanoparticulate Conjugated Microporous Polymer with Post-Modified Benzils for Enhanced Pseudocapacitor Performance. *Chem. Eur. J.* **2020**, *26*, 12343–12348. [[CrossRef](#)]
35. Liu, X.; Liu, C.-F.; Lai, W.-Y.; Huang, W. Porous Organic Polymers as Promising Electrode Materials for Energy Storage Devices. *Adv. Mater. Technol.* **2020**, *5*, 2000154. [[CrossRef](#)]
36. Luo, L.-W.; Zhang, C.; Xiong, P.X.; Zhao, Y.B.; Ma, W.Y.; Chen, Y.; Zeng, J.H.; Xu, Y.; Jiang, J.-X. A redox-active conjugated microporous polymer cathode for high-performance lithium/potassium-organic batteries. *Sci. China Ser. B Chem.* **2021**, *64*, 72–81. [[CrossRef](#)]
37. Wang, H.; Cheng, Z.; Liao, Y.; Li, J.; Weber, J.; Thomas, A.; Faul, C.F.J. Conjugated Microporous Polycarbazole Networks as Precursors for Nitrogen-Enriched Microporous Carbons for CO₂ Storage and Electrochemical Capacitors. *Chem. Mater.* **2017**, *29*, 4885–4893. [[CrossRef](#)]
38. Wang, B.; Xie, Z.; Li, Y.; Yang, Z.; Chen, L. Dual-Functional Conjugated Nanoporous Polymers for Efficient Organic Pollutants Treatment in Water: A Synergistic Strategy of Adsorption and Photocatalysis. *Macromolecules* **2018**, *51*, 3443–3449. [[CrossRef](#)]
39. Zhu, J.; Yang, C.; Lu, C.; Zhang, F.; Yuan, Z.; Zhuang, X. Two-Dimensional Porous Polymers: From Sandwich-like Structure to Layered Skeleton. *Acc. Chem. Res.* **2018**, *51*, 3191–3202. [[CrossRef](#)]
40. Li, Y.; Zheng, S.; Liu, X.; Li, P.; Sun, L.; Yang, R.; Wang, S.; Wu, Z.-S.; Bao, X.; Deng, W. Conductive Microporous Covalent Triazine-Based Framework for High-Performance Electrochemical Capacitive Energy Storage. *Angew. Chem. Int. Ed.* **2017**, *57*, 7992–7996. [[CrossRef](#)]
41. Mohamed, M.G.; Elsayed, M.H.; Elewa, A.M.; El-Mahdy, A.F.M.; Yang, C.-H.; Mohammed, A.A.K.; Chou, H.-H.; Kuo, S.-W. Pyrene-containing conjugated organic microporous polymers for photocatalytic hydrogen evolution from water. *Catal. Sci. Technol.* **2021**, *11*, 2229–2241. [[CrossRef](#)]

42. Wang, T.-X.; Liang, H.-P.; Anito, D.A.; Ding, X.; Han, B.-H. Emerging applications of porous organic polymers in visible-light photocatalysis. *J. Mater. Chem. A* **2020**, *8*, 7003–7034. [[CrossRef](#)]
43. Schmidt, J.; Werner, M.; Thomas, A. Conjugated Microporous Polymer Networks via Yamamoto Polymerization. *Macromolecules* **2009**, *42*, 4426–4429. [[CrossRef](#)]
44. Yusran, Y.; Fang, Q.; Valtchev, V. Electroactive Covalent Organic Frameworks: Design, Synthesis, and Applications. *Adv. Mater.* **2020**, *32*, e2002038. [[CrossRef](#)] [[PubMed](#)]
45. Buyukcakir, O.; Ryu, J.; Joo, S.H.; Kang, J.; Yuksel, R.; Lee, J.; Jiang, Y.; Choi, S.; Lee, S.H.; Kwak, S.K.; et al. Lithium Accommodation in a Redox-Active Covalent Triazine Framework for High Areal Capacity and Fast-Charging Lithium-Ion Batteries. *Adv. Funct. Mater.* **2020**, *30*, 2003761. [[CrossRef](#)]
46. Dai, C.; Zhong, L.; Gong, X.; Zeng, L.; Xue, C.; Li, S.; Liu, B. Triphenylamine based conjugated microporous polymers for selective photoreduction of CO₂ to CO under visible light. *Green Chem.* **2019**, *21*, 6606–6610. [[CrossRef](#)]
47. Mei, L.; Wei, J.-C.; Duan, Q. Construction of copper porphyrin-linked conjugated microporous polymer/carbon nanotube composite as flexible electrodes for supercapacitors. *J. Mater. Sci. Mater. Electron.* **2021**, *32*, 24953–24963. [[CrossRef](#)]
48. Lee, J.-S.M.; Cooper, A.I. Advances in Conjugated Microporous Polymers. *Chem. Rev.* **2020**, *120*, 2171–2214. [[CrossRef](#)]
49. Jiao, R.; Zhang, W.; Sun, H.; Zhu, Z.; Yang, Z.; Liang, W.; Li, A. N- and S-doped nanoporous carbon framework derived from conjugated microporous polymers incorporation with ionic liquids for efficient oxygen reduction reaction. *Mater. Today Energy* **2020**, *16*, 100382. [[CrossRef](#)]
50. Zhu, Z.; Yang, Z.; Fan, Y.; Liu, C.; Sun, H.; Liang, W.; Li, A. Calcination of Porphyrin-Based Conjugated Microporous Polymers Nanotubes As Nanoporous N-Rich Metal-Free Electrocatalysts for Efficient Oxygen Reduction Reaction. *ACS Appl. Energy Mater.* **2020**, *3*, 5260–5268. [[CrossRef](#)]
51. Shi, L.; Qi, Z.; Peng, P.; Guo, J.; Wan, G.; Cao, D.; Xiang, Z. Pyrene-Based Covalent Organic Polymers for Enhanced Photovoltaic Performance and Solar-Driven Hydrogen Production. *ACS Appl. Energy Mater.* **2018**, *1*, 7007–7013. [[CrossRef](#)]
52. El-Mahdy, A.F.M.; Elewa, A.M.; Huang, S.W.; Chou, H.H.; Kuo, S.W. Dual-Function Fluorescent Covalent Organic Frameworks: HCl Sensing and Photocatalytic H₂ Evolution from Water. *Adv. Opt. Mater.* **2020**, *8*, 2000641. [[CrossRef](#)]
53. Kotp, M.G.; El-Mahdy, A.F.; Yang, T.-L.; Kuo, S.-W. A pyridinyl-phenazine conjugated microporous polymer decorated with ultrafine Ag nanoparticles mediates the rapid reduction of nitrophenol. *Microporous Mesoporous Mater.* **2022**, *331*, 111669. [[CrossRef](#)]
54. Byun, J.; Zhang, K.A.I. Designing conjugated porous polymers for visible light-driven photocatalytic chemical transformations. *Mater. Horizons* **2020**, *7*, 15–31. [[CrossRef](#)]
55. Zhang, C.; Pan, G.; He, Y. Conjugated microporous organic polymer as fluorescent chemosensor for detection of Fe³⁺ and Fe²⁺ ions with high selectivity and sensitivity. *Talanta* **2021**, *236*, 122872. [[CrossRef](#)] [[PubMed](#)]
56. Song, Y.; Lan, P.C.; Martin, K.; Ma, S. Rational design of bifunctional conjugated microporous polymers. *Nanoscale Adv.* **2021**, *3*, 4891–4906. [[CrossRef](#)]
57. Zeng, W.; Zhang, Y.; Zhao, X.; Qin, M.; Li, X.; Jin, W.; Zhang, D. One-pot synthesis of conjugated microporous polymers based on extended molecular graphenes for hydrogen storage. *Polymer* **2019**, *174*, 96–100. [[CrossRef](#)]
58. Gao, R.; Zhang, G.; Lu, F.; Chen, L.; Li, Y. Pyrrole-Based Conjugated Microporous Polymers as Efficient Heterogeneous Catalysts for Knoevenagel Condensation. *Front. Chem.* **2021**, *9*, 687183. [[CrossRef](#)]
59. Roh, D.-H.; Shin, H.; Kim, H.-T.; Kwon, T.-H. Sono-Cavitation and Nebulization-Based Synthesis of Conjugated Microporous Polymers for Energy Storage Applications. *ACS Appl. Mater. Interfaces* **2021**, *13*, 61598–61609. [[CrossRef](#)]
60. Yan, C.; Meng, N.; Lyu, W.; Li, Y.; Wang, L.; Liao, Y. Hierarchical porous hollow carbon spheres derived from spirofluorene- and aniline-linked conjugated microporous polymer for phase change energy storage. *Carbon* **2020**, *176*, 178–187. [[CrossRef](#)]
61. Ma, H.; Chen, Y.; Li, X.; Li, B. Advanced Applications and Challenges of Electropolymerized Conjugated Microporous Polymer Films. *Adv. Funct. Mater.* **2021**, *31*, 2101861. [[CrossRef](#)]
62. Zhang, B.Y.; Wang, W.B.; Liang, L.N.; Xu, Z.C.; Li, X.Y.; Qiao, S.L. Prevailing conjugated porous polymers for electrochemical energy storage and conversion: Lithium-ion batteries, supercapacitors and water-splitting. *Coord. Chem. Rev.* **2021**, *436*, 213782. [[CrossRef](#)]
63. Fan, X.Y.; Chen, S.; Gong, W.B.; Meng, X.D.; Jia, Y.C.; Wang, Y.L.; Hong, S.; Zheng, L.; Zheng, L.R.; Bielawski, C.W.; et al. A Conjugated Porous Polymer Complexed with a Single-Atom Cobalt Catalyst as an Electrocatalytic Sulfur Host for Enhancing Cathode Reaction Kinetics. *Energy Storage Mater.* **2021**, *41*, 14–23. [[CrossRef](#)]
64. Zhang, H.Z.; Zhong, L.F.; Xie, J.H.; Yang, F.; Liu, X.Q.; Lu, X.H. A COF-Like N-Rich Conjugated Microporous Polytriphenylamine Cathode with Pseudocapacitive Anion Storage Behavior for High-Energy Aqueous Zinc Dual-Ion Batteries. *Adv. Mater.* **2021**, *33*, 2101857. [[CrossRef](#)]
65. Liu, Y.; Wu, S.; Gopalakrishna, T.Y.; Wu, J. Benzo[1,2-c;4,5-c']bis[1,2,5]thiadiazole-porphyrin-based near-infrared dyes. *SmartMat* **2021**, *2*, 398–405. [[CrossRef](#)]
66. Tam, T.L.D.; Wu, J. Benzo[1,2-c;4,5-c0]Bis[1,2,5]Thiadiazole in Organic Optoelectronics: A Mini-Review, Benzo[1,2-c;4,5-c0]Bis[1,2,5]Thiadiazole in Organic Optoelectronics: A Mini-Review. *J. Mol. Eng. Mater.* **2015**, *3*, 1540003. [[CrossRef](#)]
67. Tam, T.L.D.; Li, H.; Wei, F.; Tan, K.J.; Kloc, C.; Lam, Y.M.; Mhaisalkar, S.G.; Grimsdale, A.C. One-Pot Synthesis of 4,8-Dibromobenzo[1,2-c;4,5-c']bis[1,2,5]thiadiazole. *Org. Lett.* **2010**, *12*, 3340–3343. [[CrossRef](#)]

68. Du, X.; Qi, J.; Zhang, Z.; Ma, D.; Wang, Z.Y. Efficient Non-doped Near Infrared Organic Light-Emitting Devices Based on Fluorophores with Aggregation-Induced Emission Enhancement. *Chem. Mater.* **2012**, *24*, 2178–2185. [[CrossRef](#)]
69. Krieg, L.; Zhang, Z.; Splith, D.; von Wenckstern, H.; Grundmann, M.; Wang, X.; Gleason, K.K.; Voss, T. Controlled formation of Schottky diodes on n-doped ZnO layers by deposition of p-conductive polymer layers with oxidative chemical vapor deposition. *Nano Express* **2020**, *1*, 010013. [[CrossRef](#)]
70. Simon, P.; Gogotsi, Y. Materials for electrochemical capacitors. *Nat. Mater.* **2008**, *7*, 845–854. [[CrossRef](#)]
71. Liu, B.; Zhang, Q.; Wang, Z.; Li, L.; Jin, Z.; Wang, C.; Zhang, L.; Chen, L.; Su, Z.-M. Nitrogen and Sulfur-Codoped Porous Carbon Nanospheres with Hierarchical Micromesoporous Structures and an Ultralarge Pore Volume for High-Performance Supercapacitors. *ACS Appl. Mater. Interfaces* **2020**, *12*, 8225–8232. [[CrossRef](#)] [[PubMed](#)]
72. Kusuma, H.D.; Rochmadi; Prasetyo, I.; Ariyanto, T. Mesoporous Manganese Oxide/Lignin-Derived Carbon for High Performance of Supercapacitor Electrodes. *Molecules* **2021**, *26*, 7104. [[CrossRef](#)] [[PubMed](#)]
73. Mohamed, M.G.; EL-Mahdy, A.F.M.; Meng, T.S.; Samy, M.M.; Kuo, S.W. Multifunctional Hypercrosslinked Porous Organic Polymers Based on Tetraphenylethene and Triphenylamine Derivatives for High-Performance Dye Adsorption and Supercapacitor. *Polymers* **2020**, *12*, 2426. [[CrossRef](#)] [[PubMed](#)]
74. Mohamed, M.G.; Sharma, S.U.; Yang, C.H.; Samy, M.M.; Mohammed, A.A.K.; Chaganti, S.V.; Lee, J.T.; Kuo, S.W. Anthraquinone-Enriched Conjugated Microporous Polymers as Organic Cathode Materials for High-Performance Lithium-Ion Batteries. *ACS Appl. Energy Mater.* **2021**, *4*, 14628–14639. [[CrossRef](#)]
75. Mohamed, M.G.; Chen, W.C.; El-Mahdy, A.F.M.; Kuo, S.W. Porous organic/inorganic polymers based on double-decker silsesquioxane for high-performance energy storage. *J. Polym. Res.* **2021**, *28*, 219. [[CrossRef](#)]
76. El-Mahdy, A.F.M.; Kuo, S.W.; Alshehri, A.A.; Kim, J.; Young, C.; Yamauchi, Y.; Kuo, S.W. Strategic design of triphenylamine- and triphenyltriazine-based two-dimensional covalent organic frameworks for CO₂ uptake and energy storage. *J. Mater. Chem. A* **2018**, *6*, 19532–19541. [[CrossRef](#)]